# Characterization of the Terra Nova Bay Polynya Using Dual-Polarimetric C-Band SAR Measurements

Giovanna Inserra, *Student Member, IEEE*, Andrea Buono, *Senior Member, IEEE*, Ferdinando Nunziata, *Senior Member, IEEE*, Maurizio Migliaccio, *Fellow, IEEE*, Flavio Parmiggiani, and Giuseppe Aulicino

***Abstract*—In polar regions, coastal polynyas are key drivers for climate since they represent the primary source of ice mass production and oceanic circulation. In this study, multipolarization C-band synthetic aperture radar (SAR) measurements acquired by the Radarsat-2 satellite mission are exploited to observe the Terra Nova Bay (TNB) coastal polynya in the Ross Sea, Antarctica. Incoherent and coherent features, extracted from dual-polarimetric SAR measurements, are used to characterize the TNB coastal polynya under different environmental conditions. The analysis is also supported, when available, by independent optical remote sensing information collected by the thermal infrared channels of the moderate resolution imaging spectroradiometer and by ancillary on-site information about wind and air temperature collected by automatic weather stations. Experimental results show that the SAR plays a key role in providing information about the TNB polynya thanks to its fine spatial resolution and its almost continuous imaging capabilities. In addition, dual-polarimetric SAR offers unprecedented opportunities with respect to single-polarization SAR in performing accurate and unsupervised classification of the area within the polynya. Hence, a more accurate estimation of the polynya extent and the fractional area coverage of sea water within the polynyas obtained.**

***Index Terms*—Synthetic aperture radar (SAR), polarimetry, coastal polynya, Terra Nova Bay (TNB), sea ice.**

Manuscript received 17 December 2021; revised 4 November 2022 and 13 October 2023; accepted 16 January 2024. This work was supported in part by the European Space Agency (ESA) under the ESA-MOST (Chinese Ministry of Science and Technology) Dragon-5 cooperation project ID 57979 entitled "Monitoring harsh coastal environments and ocean surveillance using radar remote sensing", in part by the Italian Ministry of University and Research (MIUR) under the Antarctica National Research Programme (PNRA) entitled "Sea ice-wave interaction monitoring for marginal ice navigation." *(Corresponding author: Flavio Parmiggiani.)*

**Associate Editor: E. W. Gill.**

Giovanna Inserra, Andrea Buono, and Ferdinando Nunziata are with the Dipartimento di Ingegneria, Università degli Studi di Napoli "Parthenope", 80143 Napoli, Italy (e-mail: giovanna.inserra@ieee.org; andrea.buono@uniparthenope.it; ferdinando.nunziata@uniparthenope.it).

Maurizio Migliaccio is with the Dipartimento di Ingegneria, Università degli Studi di Napoli "Parthenope", 80143 Napoli, Italy, and also with the Istituto Nazionale di Geofisica e Vulcanologia, Sezione Osservazione della Terra, 00143 Rome, Italy (e-mail: maurizio.migliaccio@uniparthenope.it).

Flavio Parmiggiani is with Consiglio Nazionale delle Ricerche, Istituto di Scienze dell'Atmosfera e del Clima, 40129 Bologna, Italy (e-mail: f.parmiggiani@isac.cnr.it).

Giuseppe Aulicino is with Dipartimento di Scienze e Tecnologie, Università degli Studi di Napoli "Parthenope", 80143 Napoli, Italy, and also with the Consiglio Nazionale delle Ricerche, Istituto di Scienze dell'Atmosfera e del Clima, 40129 Bologna, Italy (e-mail: giuseppe.aulicino@uniparthenope.it).

Digital Object Identifier 10.1109/JOE.2024.3356569

## I. Introduction

COASTAL or latent heat polynyas are persistent and large open water areas (typically 100–500 km alongshore by 10–100 km offshore) that—mostly in polar regions—extend from the continental ice appearing as holes in the surrounding sea ice [1]. Antarctic coastal polynyas are often forced, during the winter season, by strong and cold katabatic winds that, influenced by the local topography, blow seaward pushing the pack ice offshore. Open sea water exposed to cold winds results in a fast formation of new thin ice that, at once, is pushed far from the coast as it forms. Katabatic winds prevent sea ice from consolidating as a thick pack, facilitating the continuous polynya formation, and opening by leaving the relatively warm open water exposed to the cold atmosphere [2]. The ice formation and transportation in coastal polynyas is ruled by the Langmuir circulation resulting from the wave-wind stress interaction [1]. When the newly formed sea ice is pushed away from the coast, i.e., during the opening phase of the polynya, a mixture of sea water and frazil, grease and pancake ice, also termed as active frazil, aligns as ice streaks parallel to the wind direction [3], [4], [5]. According to wind field and sea state conditions, different sea-ice types may form and accumulate along the edges of coastal polynyas.

The presence/absence of sea ice in coastal polynyas is extremely relevant for both physical and ecological aspects. First of all, it conditions the ocean–atmosphere energy, mass, gas, and momentum exchange [6]. For example, an ice-free polynya calls for an air–sea heat exchange which is one or two orders of magnitude larger than the one through the surrounding pack ice [7]. In addition, the presence and evolution of sea-ice cover represents one of the largest seasonal changes on the planet. Hence, since coastal polynyas are sea-ice production sites, knowledge about sea-ice extent within the polynya provides essential information on the salt fluxes associated with ice formation that assist convection phenomena and modulate the global ocean overturning processes [6].

In Antarctica, coastal polynyas are one of the primary sea-ice mass production (it was estimated that about 10% of the Southern Ocean sea ice comes from the main Antarctic coastal polynyas [8]) and, therefore, they play a key role in the formation of the Antarctic bottom water (AABW) and in driving the oceanic circulation of the southern hemisphere [9], [10], [11]. Coastal polynyas monitoring is of paramount interest to better understanding—among others—the ocean–ice–atmosphere

interactions and to study the Southern Ocean overturning circulation due to the densest ocean water mass, i.e., the AABW formation [2], [12], [13]. Nevertheless, harsh conditions and limited solar illumination make Antarctica coastal regions mostly inaccessible places. Thus, satellite remote sensing represents an essential and irreplaceable tool to get information on Antarctic coastal polynyas [14]. Optical sensors, especially those operating in the thermal infrared and visible frequency range of the electromagnetic spectrum, are commonly used to guarantee finer resolution (in the order of hundreds of meters) observations with a "potentially" dense enough revisit time [15], [16]. However, solar illumination and cloud coverage may severely limit the availability of such measurements and, therefore, degrade their effective revisit time. Nowadays, passive microwave radiometers represent the reference satellite sensors to get information on polynyas in Antarctica [5], [8], [10], [17], [18], [19], [20], [21]. They provide all-weather and all-day large-scale observations of polynyas with a very dense temporal sampling and, therefore, they are routinely used to obtain added-value products as the polynya extent and the sea-ice thickness, production and concentration. The special sensor microwave/imager (SSM/I) and the advanced microwave scanning radiometer for EOS (AMSR-E) have been extensively used to monitor the most significant coastal polynyas in Antarctica, including the ones located in the Terra Nova Bay (TNB), Ross Sea [5], [8], [10], [19], [20]. According to the microwave radiometer observations, the TNB polynya calls for an average frazil ice area of about 900 $km^2$ [5] and an average annual sea-ice global production of about 56 $km^3$ [10]. However, the coarser radiometer spatial resolution, in the order of tens of kilometers, significantly limits its ability to provide finer spatial resolution details about the polynya and results in contamination effects on the polynya edges (e.g., signal mixtures of land and open water or thin and pack ice).

Within this framework, the synthetic aperture radar (SAR), i.e., a fine spatial resolution imaging radar, can provide complementary fine spatial resolution details. In addition, polarimetric SAR imaging modes are routinely available which, although have been shown to provide unique benefits in several applications including cryosphere, have never been used to extract information about coastal polynyas.

In this study, we focus on the TNB polynya in the Ross Sea, since it hosts one of the largest and most persistent coastal polynyas in Antarctica that, during winter, are about 1000–1300 $km^2$ large, on average [2], [22], [23]. The TNB extends from the Drygalski ice tongue southward to Cape Washington northward, hosting two of the main Antarctica permanent research stations, the Italian Mario Zucchelli, and the Korean Jang Bogo (see Fig. 1). The TNB is almost completely covered by sea ice during the winter season from March to October, while the higher temperature during the summer season makes it ice free [24]. The joint effects of strong and persistent katabatic cold winds, i.e., at least 20–25 m/s for at least 12 h, that blow up to 50 m/s from the Nansen ice sheet toward the open ocean, together with the upwelling of warm ocean water and the Drygalski ice tongue blocking action, generate and sustain the opening and growing of the polynya [25], [26]. The morphology, i.e., extent and shape, of the TNB polynya varies on a short temporal range [25]. During winter, very frequent short-term (2–5 days) polynya events alternate with less frequent longer ones (10–15 days). Nevertheless, in response to quick changes of katabatic winds, the dynamic of a single polynya event can be even shorter than 24 hours. It was also shown that the TNB polynya growing and closing rates are significantly different: slower growing rates, i.e., 50–80 $km^2$/h (even if they can reach up to 300 $km^2$/h during strong gusts), correspond to faster closing rates, i.e., 110–150 $km^2$/h [27].

To the best of our knowledge, only few studies addressed the observation of TNB polynya by means of SAR imagery [14], [27], [28], [29]. In all the studies, the polynya boundaries are manually extracted, with the exception of the automatic image processing algorithm based on anisotropic filtering and Markov random fields which is applied to fine-resolution (15 m) X-band SAR scenes under open polynya conditions in [29]. In [14], moderate-resolution (100–150 m) L- and C-band SAR data are used, together with a multisensor satellite dataset, to monitor the polynya variability. They pointed out the benefits offered by a synergistic multisource approach, including the ones provided by very frequent fine resolution SAR observations. Those outcomes were confirmed in [28], where they also found that wind speed is one of the main driving factor affecting polynya dynamics. In [27], moderate-to-fine resolution (150–5 m) C- and X-band SAR data are enriched with ice surface temperature (IST) obtained from thermal infrared sensors to get spatio-temporal information on the polynya variability under growing and closing conditions. The COSMO-SkyMed constellation revisit time is dense enough to observe fast changes in the polynya patterns. In addition, the fine spatial resolution of SAR imagery emphasized the presence, during the growing phase, of frazil ice streaks spaced from $\approx$ 300–800 m that tend to accumulate along the surrounding sea-ice edge.

In this study, the benefits of multipolarization SAR measurements to observe the TNB polynya are discussed using a dataset of dual-polarimetric (DP) HH+HV (horizontal transmit/horizontal receive and horizontal transmit/vertical receive, respectively) C-band Radarsat-2 (RS-2) SAR measurements. Coherent and incoherent polarimetric features extracted from DP SAR measurements are used to provide scattering-based information about the TNB coastal polynya under different conditions. Experimental results point out that coherent polarimetric features provide additional information that can be used to: 1) better distinguish ice-infested areas within the open polynya; 2) quantify the amount of sea ice within the sea water polynya area during the largest sea-ice production activity period; 3) better estimate of the polynya extent and the fractional area coverage of sea water in a very effective and unsupervised way, under different polynya conditions. This means that SAR polarimetric modes offer unique benefits with respect to the single-polarization counterpart to improve the understanding of the complex polynya environment.

The rest of this article is organized as follows. A primer on SAR polarimetry is provided in Section II, and the dataset is presented in Section III, while experimental results are shown and discussed in Section IV. Finally, Section V concludes this article.

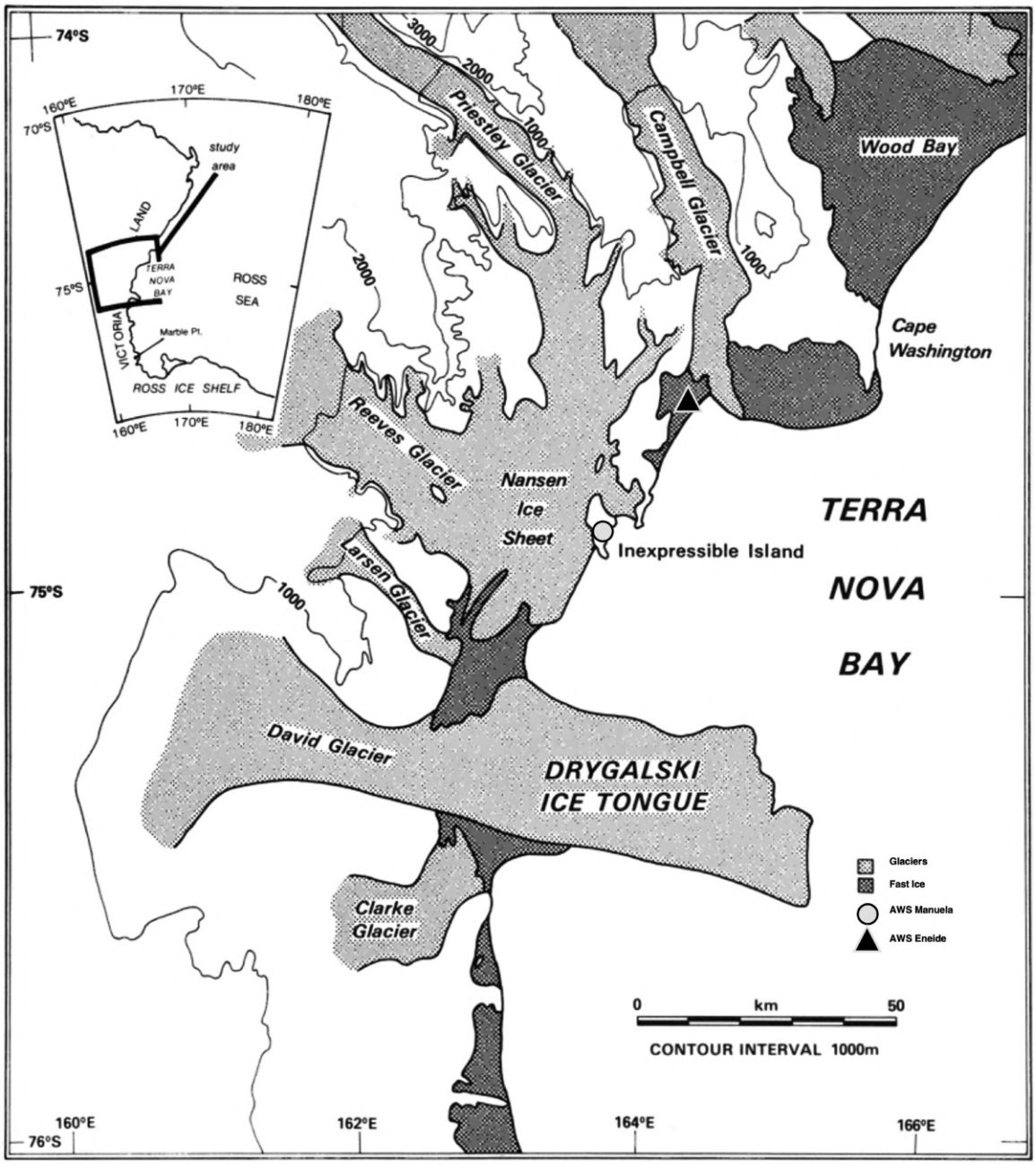


Fig. 1. Study area: Terra Nova Bay (adapted from [22]). The location of "Manuela" and "Eneide" automatic weather stations (AWSs) are also marked as a gray circle and a black triangle, respectively.

## II. Primer on SAR Polarimetry

The polarimetric SAR measures, for each resolution cell, the scattering matrix of the observed scene. Among the different polarimetric imaging modes, DP represents a good compromise between hardware complexity and amount of scattering information. It typically consists of transmitting a single linearly polarized (horizontal - H, or vertical - V) electromagnetic wave while receiving, coherently, under the orthogonal H–V polarization basis. DP SAR systems do not measure the complete scattering matrix as in the fully polarimetric case and, therefore, the partial nature of DP SAR measurements limits the amount of scattering information that can be extracted from actual data in a way that depends on the particular application [30], [31], [32].

To provide a physical understanding of polarimetric SAR measurements, second-order descriptors are needed. Among the latter, the covariance matrix, i.e., a complex-valued $2 \times 2$ Hermitian and semidefinite positive matrix is often used [32]

$$\mathbf{C} = \begin{pmatrix} \mathbf{C}_{11} & \mathbf{C}_{12} \\ \mathbf{C}_{21} & \mathbf{C}_{22} \end{pmatrix} = \begin{pmatrix} \langle S_{xx} S_{xx}^* \rangle & \langle S_{xx} S_{xy}^* \rangle \\ \langle S_{xy} S_{xx}^* \rangle & \langle S_{xy} S_{xy}^* \rangle \end{pmatrix} \tag{1}$$

where $\langle\cdot\rangle$ stands for ensemble average, the superscript $^*$ means complex conjugate and each $S_{ij}$, with $\{i,j\}\in\{\mathrm{H},\mathrm{V}\}$, is termed as scattering amplitude. The DP covariance matrix allows extracting several features associated with the backscattering properties of the observed scene that can be grouped into incoherent and coherent features. The former include the co- and cross-polarized normalized radar cross sections (NRCSs) and the total backscattered power, namely, the SPAN

$$\sigma^0_{xx}=\mathbf{C}_{11}=\langle|S_{xx}|^2\rangle,\quad \sigma^0_{xy}=\mathbf{C}_{22}=\langle|S_{xy}|^2\rangle$$
$$\mathrm{SPAN}=\mathbf{C}_{11}+\mathbf{C}_{22}=\sigma^0_{xx}+\sigma^0_{xy} \tag{2}$$

When dealing with DP coherent features, a typical approach consists of exploiting the spectral properties of the covariance matrix through the eigen-decomposition that provides two child parameters, namely, the polarimetric entropy $H$ and mean scattering angle $\bar{\alpha}$ [33]

$$0\le H=-\sum_{i=1}^{2}\frac{\lambda_i}{\lambda_1+\lambda_2}\log_2\frac{\lambda_i}{\lambda_1+\lambda_2}\le 1$$
$$0^\circ\le\bar{\alpha}=\sum_{i=1}^{2}\frac{\lambda_i}{\lambda_1+\lambda_2}\cos\left(|\boldsymbol{u}_1(i)|\right)^{-1}\le 90^\circ. \tag{3}$$

In (3), $\lambda_1$ and $\lambda_2$ are the real and nonnegative eigenvalues of $\mathbf{C}$ satisfying $\lambda_1\ge\lambda_2\ge 0$, $\boldsymbol{u}_1$ is the first, complex orthogonal eigenvector of $\mathbf{C}$. $H$, bounded in the range [0, 1], is related to the degree of randomness of the polarization state of the backscattered wave, with $H$ values close to 0 (1) referring to fully polarized (completely depolarized) backscattered waves. The mean scattering angle $\bar{\alpha}$, bounded in the range [0°, 90°], represents the average phase related to the scattering mechanisms represented by the eigenvectors, with $\bar{\alpha}$ values close to 0° (90°) being associated with single-reflection (double-reflection) surface scattering mechanisms, while $\bar{\alpha}$ values close to 45° refer to multiple-reflection volume scattering.

To describe the main scattering mechanisms occurring within the polynya, two different scenarios must be accounted for: sea-ice-free and sea-ice-infested water. In the former one, the sea surface scattering mechanism is well described by the Bragg/tilted-Bragg model that results in a quasi-deterministic, i.e., low entropy and low mean scattering angle, polarimetric scattering [34], [35]. In the sea-ice-infested scenario, completely different polarimetric scattering properties are expected due to the different dielectric and roughness properties that characterize ice-infested areas. The latter exhibit a large variability according to thickness, roughness, and composition (water volume fraction, snow/brine layer, etc.) of sea ice. Although the characterization of polarimetric scattering from sea ice is a very nontrivial task [36], [37], for the purpose of this study, it is worth noting that sea-ice-free polarimetric scattering is expected to be well-distinguishable from the ice-infested one due to the large amount of depolarization and multiple interactions resulting from the complex ice environment. Hence, in case of sea ice, large $H$ and $\bar{\alpha}$ values are to be expected. Following this rationale, the $H$ and $\bar{\alpha}$ parameters are here used to classify the polynya using the Wishart classifier, which has been successfully used for both land and sea applications [39], [40], [41]. The rationale consists of partitioning the so-called $H$-$\bar{\alpha}$ plane into regions that admit a physical scattering interpretation. For instance, in [38] eight regions are defined that span from quasi-deterministic Bragg surface scattering (i.e, $H\le 0.5$ and $\bar{\alpha}\le 42^\circ$) up to random volume scattering.

The interpretation of the regions in terms of physical scattering mechanisms is only possible when full-polarimetric SAR measurements are available. In this study, DP SAR measurements are available; therefore, a suboptimal classification scheme can be implemented which does not allow a straightforward interpretation of the classes in terms of physical scattering mechanisms [30], [31], [32]. However, since the ice-free and ice-infested scattering are expected to be well-distinguishable in the polarimetric space, it is worth expecting that they will be classified into different regions by the Wishart classifier.

## III. Dataset

The SAR dataset consists of three C-band RS-2 single-look complex (SLC) high-quality (low noise equivalent sigma zero) SAR scenes collected in descending pass in HH-HV DP wide fine imaging mode and covering different polynya conditions. The first SAR scene was collected at the end of Antarctica winter season, on September 15, 2014, where the TNB polynya is at its maximum, i.e., it calls for a large ice-free area along with a significant sea-ice production and an increased salinity in the water column [11]. The second SAR scene was collected at the end of summer season, on March 2, 2015, where a "partial" polynya activity can be observed, i.e., the polynya is still active but the TNB is only partially ice-free and the salinity in the water column is decreasing [11]. The third SAR scene was collected during Antarctica summer season, on February 6, 2016, when the area of interest is almost ice-free and, therefore, no polynya can be observed. Each SAR image covers a wide area of about 165 × 165 km with a spatial resolution of 4.7 m × 5.4 (range × azimuth) and is collected under an incidence angle that spans from 19° to 31°. Excerpts of SAR scenes including the TNB coastal region, observed at an incidence angle of about 25°, are considered that cover an area of about 45 × 75 km. Those excerpts were radiometrically calibrated, georeferenced, and processed to get a pixel spacing of 11.64 × 5.40 m (range × azimuth). In addition, the images were speckle filtered, using a 5 × 5 sliding window, to improve the estimation of polarimetric features. The corresponding multipolarization NRCS graytones images, are shown in Fig. 2, which is arranged in a matrix format where columns refer to the different polarimetric channels (i.e., HH and HV), while rows refer to the different acquisition dates. Note that decibel (dB) unit is used. The observed area includes the TNB polynya, the land ice (see the continental ice shelf eastward), the Drygalski ice tongue (southward), and different types of sea ice. When available, independent satellite remote sensing information, i.e., space and time collocated optical imagery acquired by the Aqua MODIS mission at 1-km spatial resolution, are used for reference purposes. The cloud-free thermal MODIS imagery within 12 h from the SAR acquisition, are used to obtain IST information on the TNB area, from which the polynya extent

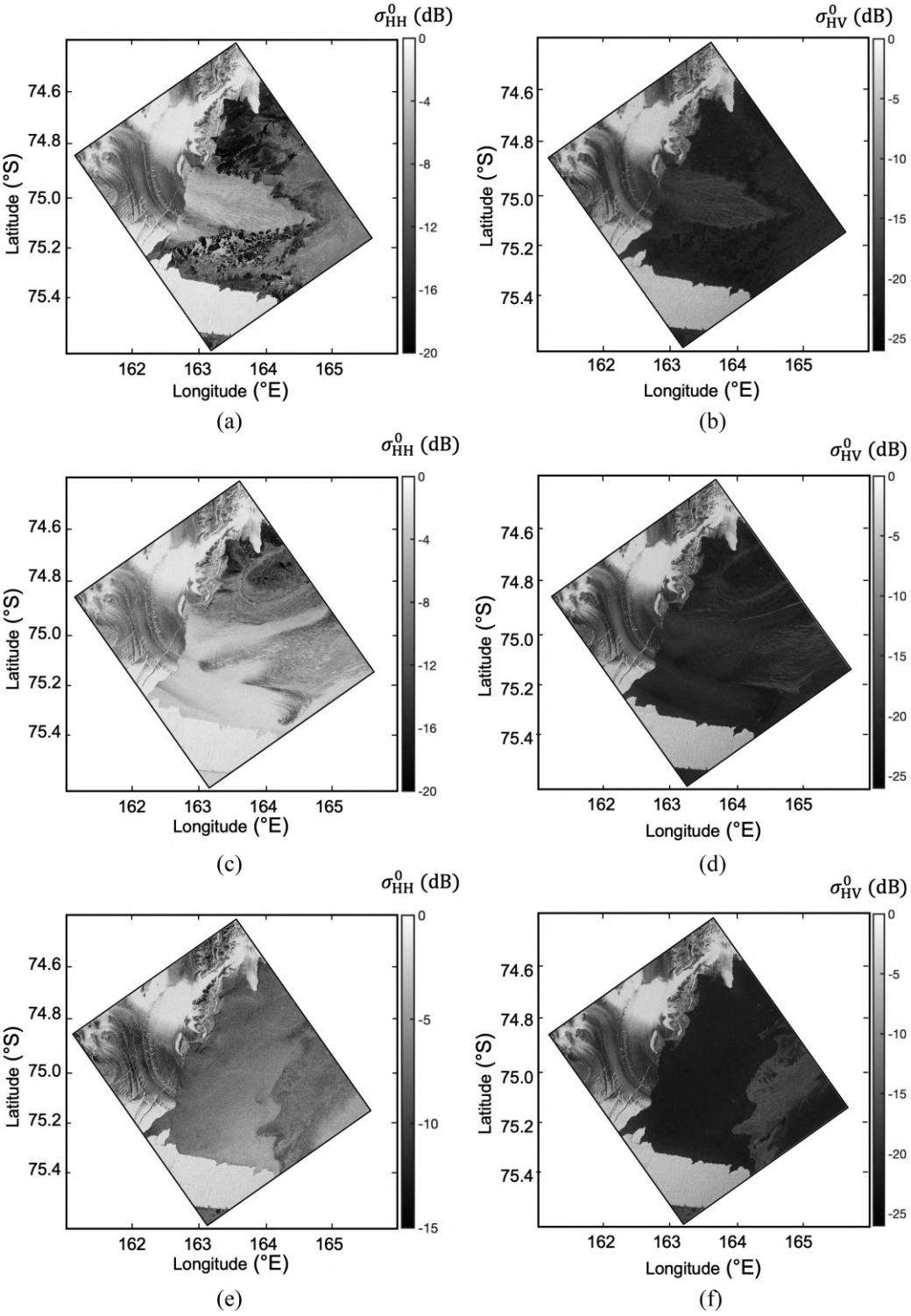


Fig. 2. Multipolarization NRCS graytones images, in dB scale, relevant to the TNB polynya. Rows refer to the different acquisition dates: (a)–(b) September 15, 2014, (c)–(d) March 2, 2015, and (e)–(f) February 6, 2016; while columns refer to the different polarization channels: (a), (c) and (e) HH and (b), (d), and (f) HV.

and its actual condition, i.e., opening/closing, can be estimated according to the method developed in [25]. For the sake of completeness, the three collocated MODIS images are shown in Fig. 3, which is arranged in a matrix format where rows refer to the three SAR acquisition dates while columns refer to the emissivity channels 31 and 32 and to the IST obtained, as suggested in [25]. In fact, calibrated radiance data from MODIS infrared channels (the bands 31 and 32 call for central wavelength of 11 and 12 $\mu$m, respectively) can be converted to brightness temperatures by inverting the Planck's function. Then, IST values can be evaluated using the split-window method and including the regression coefficient set for Antarctica [25]. As shown in Fig. 3, brighter areas meaning warmer regions in the TNB are observed in the emissivity channel images relevant

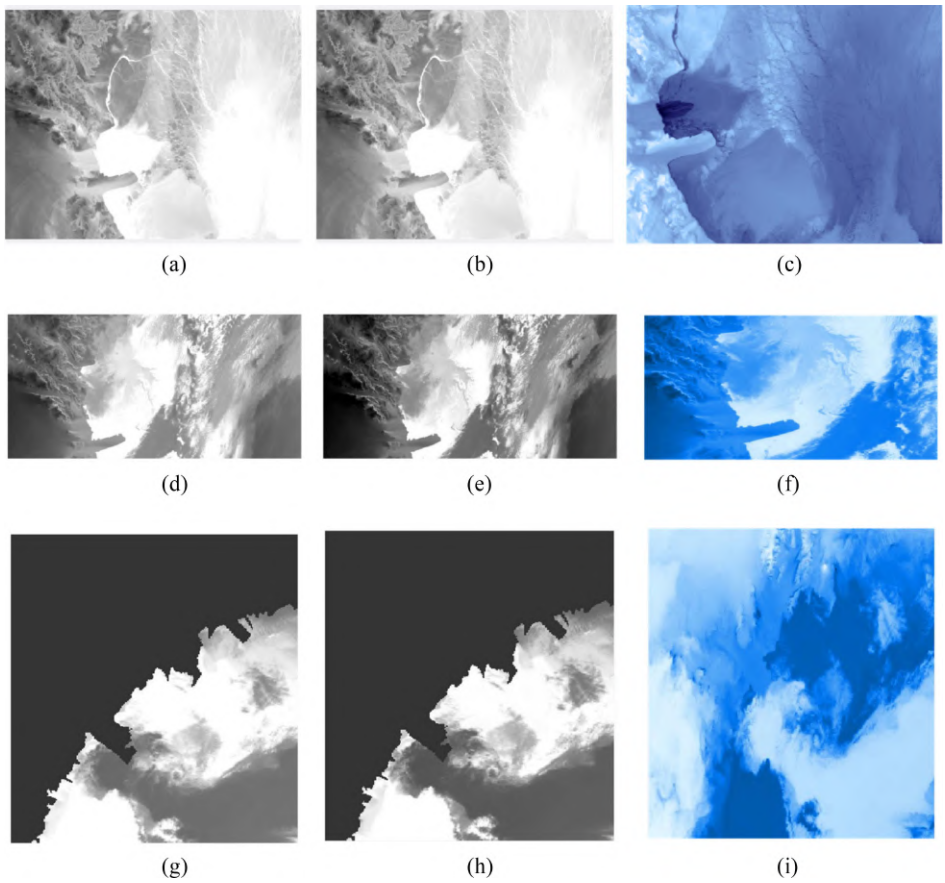


Fig. 3. Ancillary optical information from MODIS. Rows refer to images collected on September 15, 2014, March 2, 2015 and February 6, 2016; while columns refer to the emissivity channels 31 and 32, and to the IST estimated according to [25].

TABLE I
SAR AND ANCILLARY DATASETS

| SAR | RS-2 | | |
|---|---|---|---|
| Frequency | C-band (5.4 GHz) | | |
| Imaging mode | DP HH+HV | | |
| Nominal noise equivalent sigma zero (dB) | -35 | | |
| Incidence angle (°) | 19 - 31 | | |
| Orbit pass | Descending | | |
| Acquisition time (UTC) | 15:48 | | |
| Area coverage (km) | 165 × 165 | | |
| Spatial resolution, range × azimuth (m) | 4.7 × 5.4 | | |
| Automatic weather station | Manuela/Eneide | | |
| | SAR image September 15, 2014 | SAR image March 2, 2015 | SAR image February 6, 2016 |
| Air temperature at 16:00 UTC (°C) | -17.4/-17.5 | -18.3/-12.8 | -5.1/-6.4 |
| Wind speed (m/s) | 25.2/2.0 | 25.1/17.0 | 10.0/8.7 |
| Wind direction | W/WSW | W/WNW | W/WNW |
| MODIS image | Cloud-free (13:00 UTC) | Cloudy | Cloud-free (4:15 UTC) |

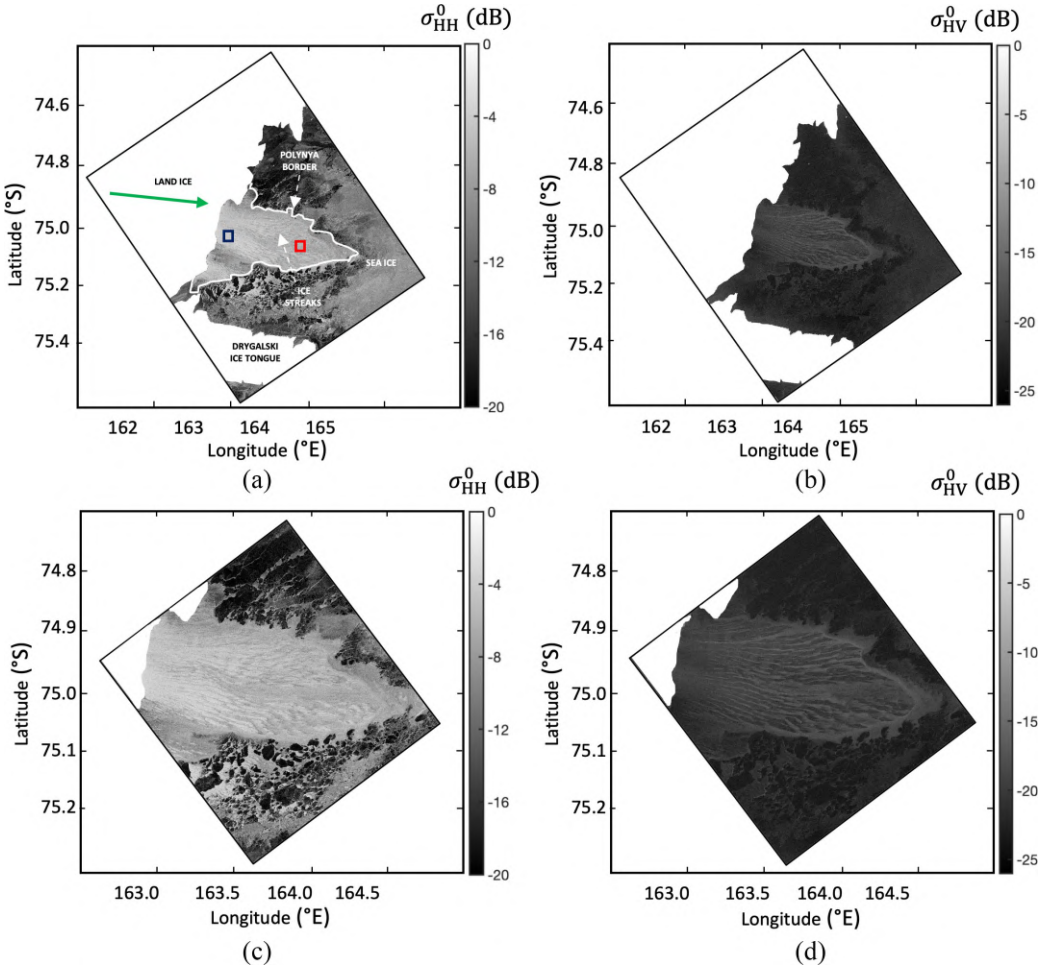


Fig. 4. Excerpts of (a) the HH and (b) the HV SAR imagery collected on September 15, 2014. In panel (a), the morphological features are annotated together with the sea water and sea-ice ROIs shown as blue and red boxes, respectively. In addition, land ice is masked out in white and a green arrow is used to show the AWS wind direction averaged over 12 hours. An enlarged version of the area that includes the polynya, imaged using the HH and HV channels, is displayed in panels (c) and (d), respectively.

to September 15, 2014 [panels (a) and (b)] and March 2, 2015 [panels (d) and (e)], witnessing an ice-free conditions, while this is no longer the case for the acquisition relevant to February 6, 2016.

In addition to optical imagery, ancillary on-site information is also collected from the automatic weather stations (AWSs) placed in the study area, i.e., "Manuela" (74° 56' 45.6" S, 163° 41' 13.2" E) and "Eneide" (74° 41' 45" S, 164° 5' 32" E), see Fig. 1. Those AWSs, placed at 78 and 91 m above sea level, respectively, are about 30 km far away from each other and provide routinely measurements of atmospheric pressure, air temperature, relative humidity, and wind vector on an hourly basis. The most important AWS parameters to characterize the TNB polynya at the SAR acquisition time are listed in Table I. It is worth noting that the two AWSs result in different parameter values that suggest a significant spatial variability of the environmental conditions in the area of interest.

The visual inspection of SAR imagery, supported by collocated IST and AWSs information, suggests the following considerations. The SAR imagery of Fig. 2(a)–(d) show a polynya in its opening phase that results in the formation of frazil ice. This is also confirmed by the recorded high winds, i.e., wind speed larger than 17 m/s, and low air temperature, i.e., below −12 °C, over the study area. The SAR imagery of Fig. 2(e)–(f) show the area in summer time and, as expected, no polynya is present. At the SAR acquisition time, a moderate wind regime applied, i.e., about 9 m/s, and an air temperature above −6 °C was recorded. Nonetheless, it is important to stress that coastal polynyas are memory-systems whose actual status depends also on the metocean conditions of the previous 12 h [11]. To summarize, all the key information on the dataset is listed in Table I.

## IV. Experiments and Discussion

In this section, the TNB polynya is analyzed using the SAR dataset and the features described in Sections II and III. The visual inspection of the SAR scenes showed that the polynya is a very complex environment whose signature in the SAR imagery changes according to both metocean conditions and the polarimetric channel. The shape of the polynya can be very well structured, as in the case of Fig. 2(a), or it can be hardly recognized, as in the case of Fig. 2(c).

The first experiment refers to the HH- and HV-polarized SAR imagery collected on September 15, 2014, see Fig. 4(a) and

TABLE II
MEAN AND STANDARD DEVIATION VALUES OF THE FEATURES EVALUATED, FOR EACH SAR IMAGE, OVER THE SELECTED ROIS SHOWN IN FIG. 2

| | | Incoherent features | | | | | | Coherent features | | | |
|---|---|---|---|---|---|---|---|---|---|---|---|
| SAR image | ROI | $\sigma^0_{HH}$ (dB) | $\sigma^0_{HV}$ (dB) | SPAN (dB) | $B_{HH}$ | $B_{HV}$ | $B_{SPAN}$ | $H$ | $\bar{\alpha}$ (°) | $B_H$ | $B_{\bar{\alpha}}$ |
| 15/9/2014 | Sea water | -4.00 ± 0.94 | -20.00 ± 1.18 | -3.88 ± 0.90 | 1.97 | 2.99 | 1.97 | 0.15 ± 0.04 | 4.40 ± 1.47 | 4.95 | 5.54 |
| | Sea ice | -6.05 ± 1.43 | -17.00 ± 1.53 | -5.71 ± 1.38 | | | | 0.36 ± 0.09 | 10.40 ± 3.26 | | |
| 2/3/2015 | Sea water | -3.24 ± 0.81 | -20.48 ± 1.20 | -3.16 ± 0.80 | – | – | – | 0.13 ± 0.03 | 3.52 ± 1.20 | – | – |
| 6/2/2016 | Sea water | -5.74 ± 1.24 | -22.03 ± 1.15 | -5.63 ± 1.21 | – | – | – | 0.15 ± 0.03 | 4.35 ± 1.02 | – | – |

Bhattacharyya distances between sea water and sea-ice pdfs are also listed for each feature.

4(b), respectively. To improve the interpretation of the SAR imagery, the most meaningful morphological features of the study area were annotated in Fig. 4(a). Land ice is masked in white and the boundary of the polynya is marked using a bold white line. Ice streaks within the polynya and the outer sea ice are also annotated. An enlarged version of the polynya area is shown in Fig. 4(c) and 4(d), where the presence of ice streaks and the polynya boundary are better visible in the graytones images. The shape of the polynya, which extends in the seaward direction almost parallel to the Drygalski ice tongue, is well recognizable both in the HH- and HV-polarized SAR imagery [Fig. 4(a) and 4(b), respectively], although remarkable differences apply. When dealing with the HH-polarized SAR image, the ice-free sea surface appears brighter than the sea-ice streaks that are aligned to the wind direction according to the underlying Langmuir ocean circulation. In the HV-polarized SAR image an opposite behavior applies with the ice streaks appearing brighter than the surrounding ice-free water. The visual inspection suggests that the two polarimetric channels carry on complementary scattering information that can be jointly exploited to better characterize TNB polynya.

The graytones images of the SPAN, the wave entropy $H$ and the mean scattering angle $\bar{\alpha}$, are shown in Fig. 5. The polynya signature can be easily distinguished in the SPAN image [see Fig. 5(a)], which also shows the thin sea-ice streaks. Within the polynya, the sea water results in a total backscattered power larger than the sea ice that appears as slightly darker streaks. This behavior resembles the HH-polarized one, witnessing that copolarized backscattering dominates the total backscattering. When dealing with the entropy image, see Fig. 5(b), sea-ice-free and sea-ice-infested polynya regions call for different values, see the blue and red boxes, respectively. Within the polynya, the sea water is very dark witnessing that low entropy values apply, while thin sea ice appears as brighter streaks. Similar comments apply for the mean scattering angle, see Fig. 5(c).

To perform a quantitative analysis, the mean and the standard deviation values of incoherent and coherent features are evaluated within two equal-size regions of interests (ROIs) selected over homogeneous sea water and sea-ice areas within the polynya, see blue and red boxes in Fig. 4(a), respectively. The features values, listed in Table II, show that the sea-ice-free ROI calls for a copolarized backscattered signal that is about 2 dB

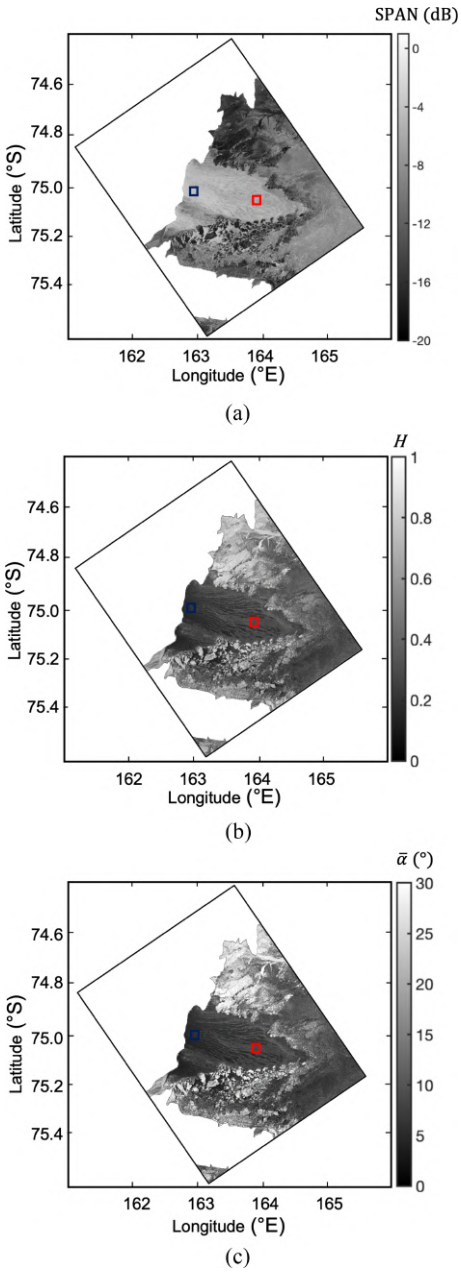


Fig. 5. Graytones images showing (a) SPAN (dB). (b) $H$. (c) $\bar{\alpha}$ (°) features. Ice-free and ice-infested water ROIs are highlighted with blue and red boxes, respectively. Land ice is masked in white.

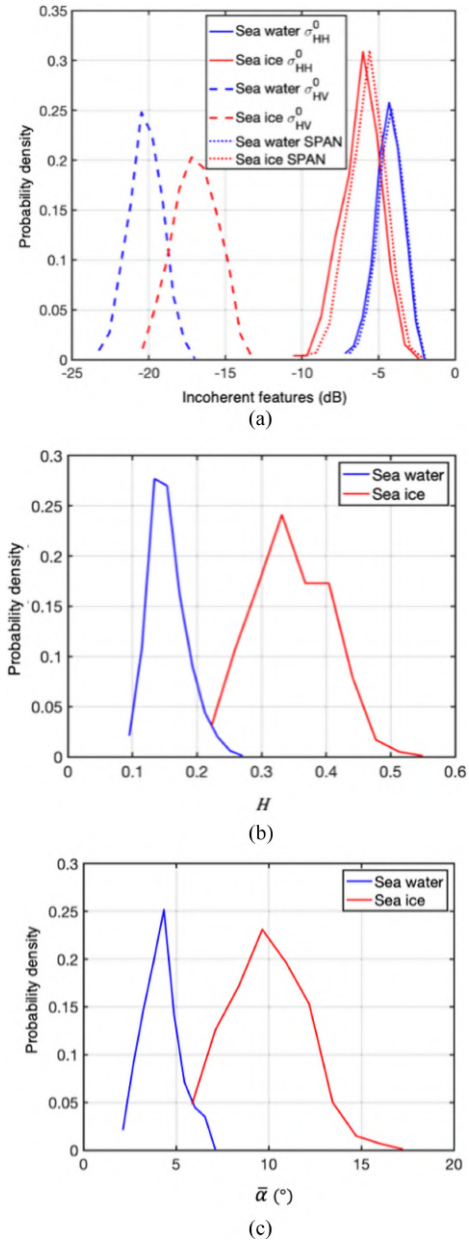


Fig. 6. Empirical pdf of the features evaluated over the selected sea water (in blue) and sea ice (in red) ROIs for: (a) incoherent features, with continuous, dashed and dotted lines referring to HH- and HV-polarized NRCS and the SPAN. Coherent (b) $H$ and (c) $\bar{\alpha}$ (°) features.

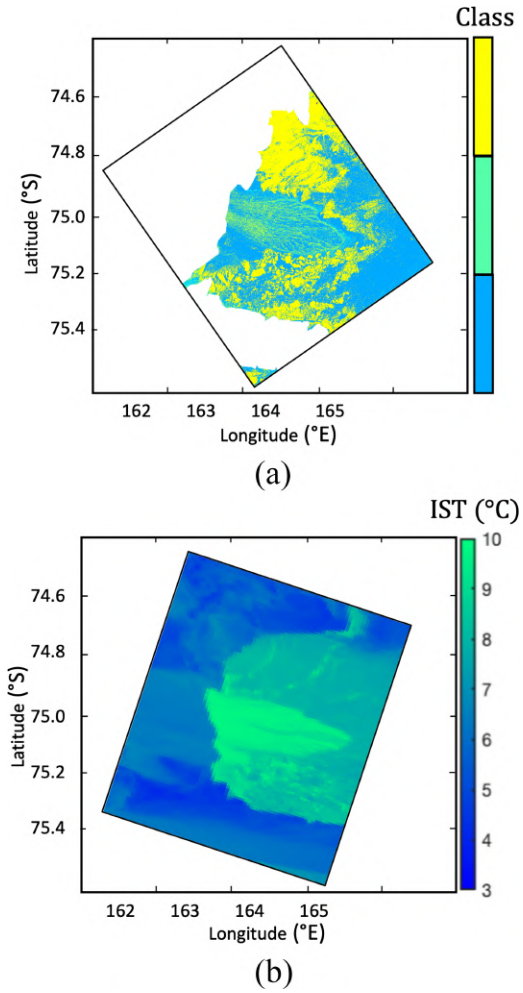


Fig. 7. Unsupervised Wishart $H/\bar{\alpha}$ classification output (a), where land ice is masked out. (b) IST image (in °C) obtained from MODIS at the SAR acquisition time.

larger than the one resulting from the sea-ice-covered ROI. This is likely due to their different surface roughness. A significantly weaker (about 13 dB lower) cross-polarized backscattering applies over both sea-ice-free and sea-ice-covered ROIs, with the sea-ice calling for an average HV-polarized NRCS about 3 dB larger than the sea-ice-free one. This is likely due to the larger volume scattering contribution resulting from the ice streaks. For both the incoherent features, the NRCS standard deviation is approximately within the range 1 to 1.5 dB, with sea-ice ROI calling for a slightly larger variability (about 0.5 dB) due to the more heterogeneous dielectric and geometric properties. The sea-ice-free ROI calls for an average SPAN approximately 2 dB larger than the iced ROI. However, the SPAN standard deviation is almost in the same range of the co- and cross-polarized NRCSs, with the sea-ice-covered ROI calling for a standard deviation about 0.5 dB larger than the one resulting from the sea-ice-free ROI. This result witnesses the intrinsic larger space variability of sea-ice streaks within the polynya with respect to the sea water. According to Table II, the sea-ice-free ROI calls for a low entropy (0.15 on average), while the iced ROI results in larger $H$ values (0.36, on average); the $\bar{\alpha}$ average values related to the ice-infested ROI are larger than the ice-free ones (on average, about 10° versus approximately 4°).

To further investigate the distinctive behavior that characterizes incoherent and coherent features, their empirical probability density function (pdf) is evaluated within the two ROIs together with the Bhattacharyya distance $B$ [42], [43], [44]

$$B = -ln\left(\sum_{x\in X}\sqrt{(s(x)w(x)}\right) \tag{4}$$

where $s$ and $w$ represent the value assumed by the considered feature in the pixel under test $x$ belonging to the sea water and sea ice ROIs, consisting of $X$ samples, respectively. Results are shown in Fig. 6 and Table II.

The pdfs of the incoherent features are shown in Fig. 6(a), where blue and red colors refer to sea water and sea ice ROIs,

TABLE III
TNB POLYNYA EXTENT

| Estimated area ($km^2$) | | | | | | | |
|---|---|---|---|---|---|---|---|
| Satellite source | | SAR | | | MODIS | | |
| ROI | | Sea water | Sea ice | Total | Sea water | Sea ice | Total |
| Acquisition date | September 15, 2014 | 743 | 287 | 1,030 | 1,428 | – | 1,428 |
| | March 2, 2015 | 1,890 | – | 1,890 | N/A | – | N/A |

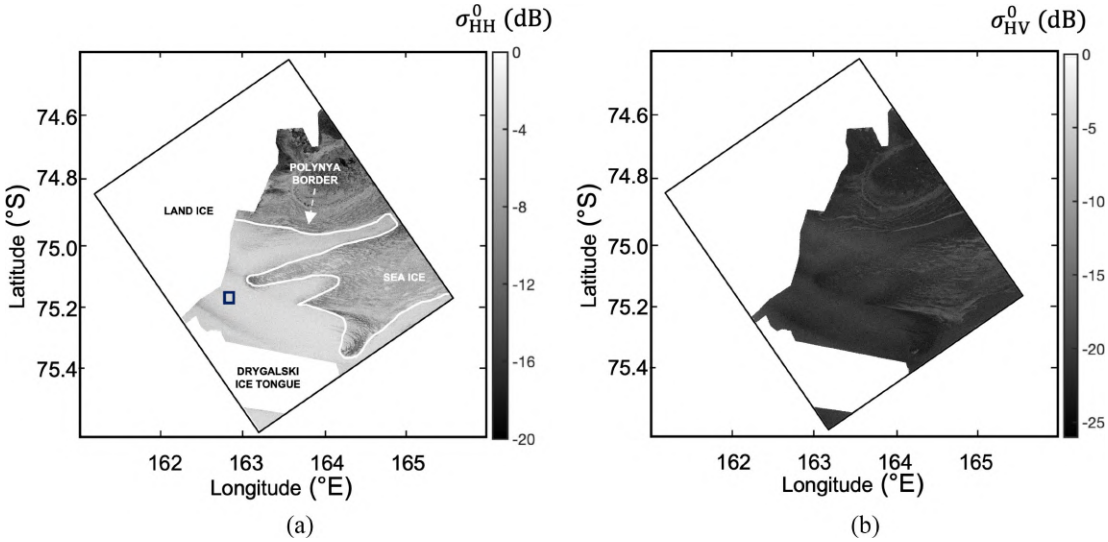


Fig. 8. Excerpts of the HH (a) and the HV (b) SAR imagery collected on March 2, 2015. The morphological features and the ROI are shown in panel (a) and the land ice is masked out using white color.

respectively, while continuous, dashed, and dotted lines stand for HH- and HV-polarized NRCS and SPAN, respectively. In all the cases, the sea water and the sea-ice pdfs are partially overlapped. The SPAN and the copolarized channel call for the largest overlapping that reduces in the cross-polarized channel. This analysis suggests using the cross-polarized channel to improve the discrimination between ice-free and ice-infested sea areas. The pdfs related to coherent features, see Fig. 6(b) and 6(c), show that a better separability is achieved. This is supported by the Bhattacharyya distances larger than the previous ones, see Table II. The separability achieved with $H$ and $\bar{\alpha}$ improves of approximately 66% and 85% with respect to the HV-polarized NRCS. These results demonstrate the importance of coherent polarimetric features in improving sea-ice/water separability.

To distinguish ice-infested water from ice-free sea surface within the TNB, the Wishart $H/\bar{\alpha}$ classifier is used, whose output is displayed in Fig. 7(a). The TNB polynya area is automatically partitioned into two distinct classes displayed in light blue and bright green color. It can be noted that the two classes well fit the sea ice and the ice streaks, respectively [see Fig. 4(a)], demonstrating that the two classes call for scattering mechanisms well-distinguishable using coherent polarimetric features. The classification output also shows that the boundary of the polynya can be automatically traced. These results are also operationally interesting since they concur to a fair estimation of the sea water extent and the fractional area coverage of sea water within the polynya. Accordingly, by applying a simple masking, the total polynya area is estimated to be 1030 $km^2$, where 287 $km^2$ out of 1030 $km^2$ are covered by thin sea ice, see Table III. This means that the polynya, usually assumed as a homogeneous and completely ice-free region even in conventional SP SAR approaches (see [14], [27], [29]), consists of about 28% of sea ice. Nonetheless, it is worth noting that sea-ice streaks within the polynya consist of a mixture of sea water and frazil/grease/pancake ice [3] and, therefore, to assume that a single pixel is completely ice-free (i.e., sea water) or ice-covered (i.e., sea ice) is a simplifying but reasonable assumption at the SAR resolution scale. For reference purposes, the polynya extent is also estimated from the IST derived at the SAR acquisition time according to [25], see Fig. 7(b). The TNB area covered by the polynya, see bright green area calling for IST larger than 9 °C, is estimated to be 1428 $km^2$, i.e., about 50% more than the sea water polynya area estimated from the DP SAR. This is a key information considering that coastal polynyas represent one of the primary sea-ice mass production sources and that the sea ice significantly affects the ocean-atmosphere interaction, i.e., heat exchange, energy, mass, and momentum [19].

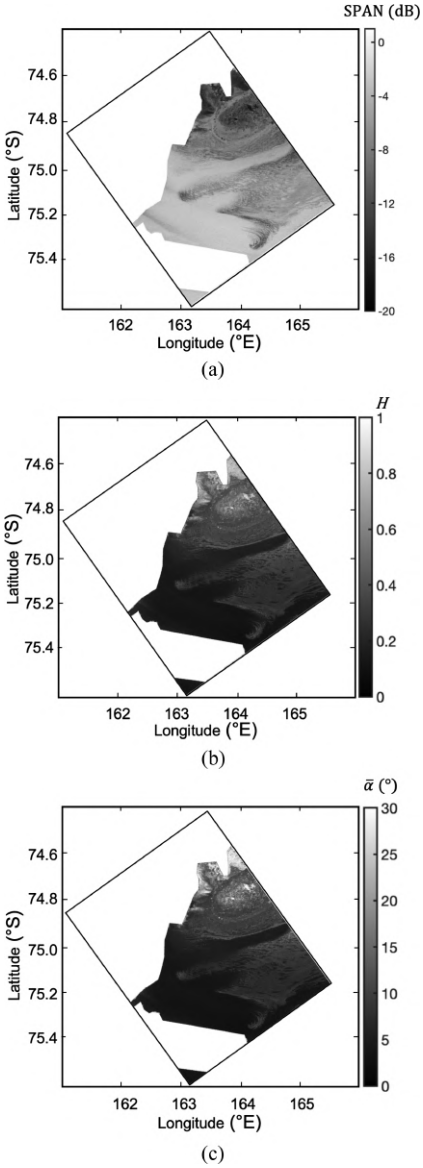


Fig. 9. Graytones images showing (a) the SPAN (dB); (b) the $H$, and (c) the $\bar{\alpha}$ (°) features. Land ice is masked in white.

The second experiment refers to the SAR scene collected on March 2, 2015, see Fig. 8, where again land ice is masked in white. In Fig. 8(a), the boundary of the polynya is visually annotated using a white line and the sea water ROI is also highlighted with a blue box. By visually inspecting the HH [Fig. 8(a)] and HV [Fig. 8(b)] images, no ice streak is visible, although the polynya is in the opening phase. The sea ice accumulates along the edge of the polynya and, therefore, the latter appears as an almost homogeneous ice-free sea surface area. The polynya can be observed in both the SAR imagery and it extends as a forked sea-water tongue brighter than the surrounding sea ice. The graytones images related to the SPAN (dB), the $H$, and the $\bar{\alpha}$ (°) features are displayed in Fig. 9(a)–(c), respectively. In all the cases, the polynya can be easily distinguished from the surroundings. The SPAN image [see Fig. 9(a)] shows that the polynya is brighter than the surrounding sea ice. In the $H$ and $\bar{\alpha}$ images [see Fig. 9(b) and 9(c)] the opposite behavior applies since the polynya is darker than both the sea ice along its edge and the surrounding environment. In this case, there is no ice streak within the polynya; hence, the quantitative analysis is carried out using the ROI selected over the sea area within the polynya. The mean and standard deviation values of the features are listed in Table II. The features call for values close to the ones measured in the first experiment, confirming that the sea within the polynya results in a dominant Bragg-like scattering behavior that calls for low depolarization.

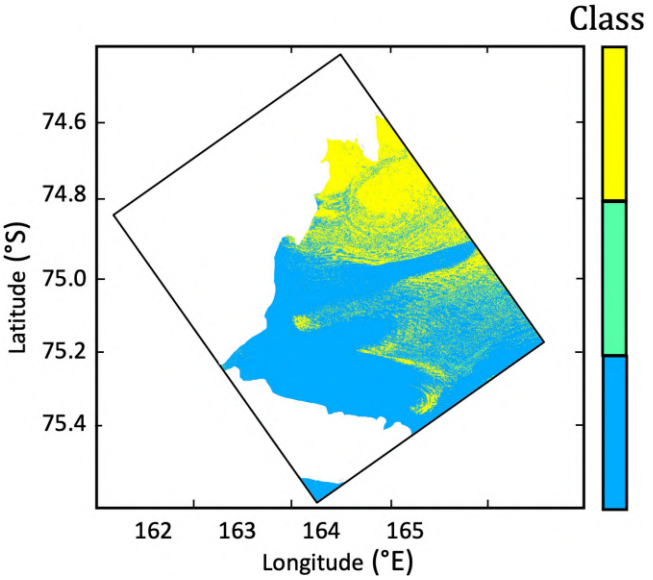


Fig. 10. Unsupervised Wishart $H/\bar{\alpha}$ output where land ice is masked in white.

The capability of coherent polarimetric features to automatically estimate the polynya extent is verified using the unsupervised Wishart $H/\bar{\alpha}$ classifier. The output, see Fig. 10, shows that the area depicted in light blue color well fits the ice-free homogeneous area within the polynya with the exception of few isolated pixels (less than 1% of the total number of pixels) that belong to a different class showing a polarimetric behavior different from the sea one. Those pixels do not show a clear pattern; hence, they can be considered as isolated and not reliable spots that can be easily sorted out when estimating the total polynya area. The latter is estimated to be equal to 1890 km$^2$, see Table III. Unfortunately, no cloud-free time collocated MODIS image is available to contrast optical and radar estimations (see Table I). Nonetheless, this stresses the fundamental role played by SAR imagery in routinely observing the TNB polynya.

The third experiment refers to the SAR scenes collected on February 6, 2016, see Fig. 11(a) and 11(b), where land ice is masked in white. In Fig. 11(a), the sea water ROI is emphasized by a blue box. By visually inspecting the images, the TNB is almost completely ice-free with the exception of some accumulated sea ice pushed offshore by the wind. This is compatible with the summer metocean conditions that are such that no polynya can be formed and sustained. The graytones

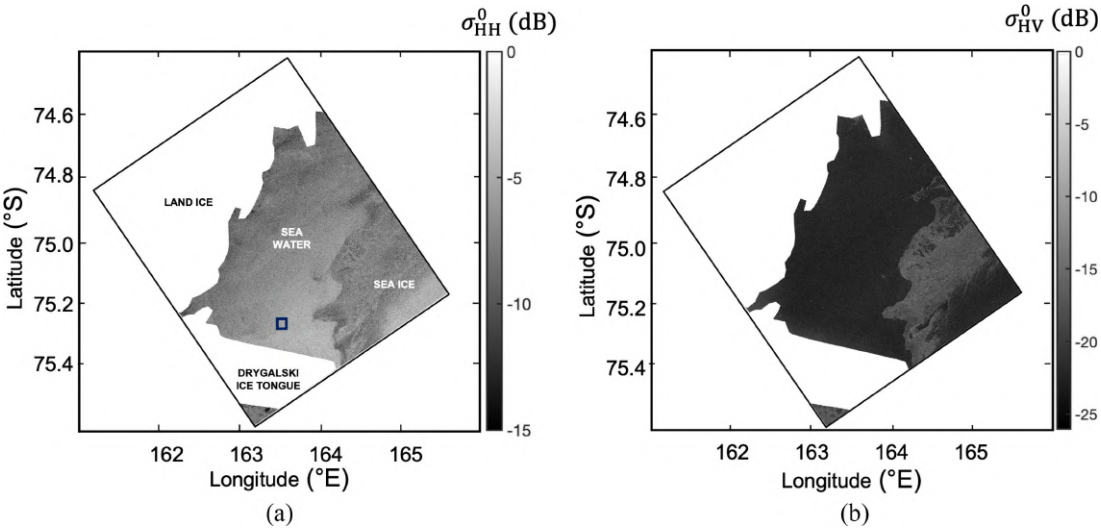


Fig. 11. Excerpts of (a) the HH and (b) the HV SAR imagery collected on February 6, 2016. In panel (a), the morphological features are annotated together with the ROI. In addition, land ice is masked out in white.

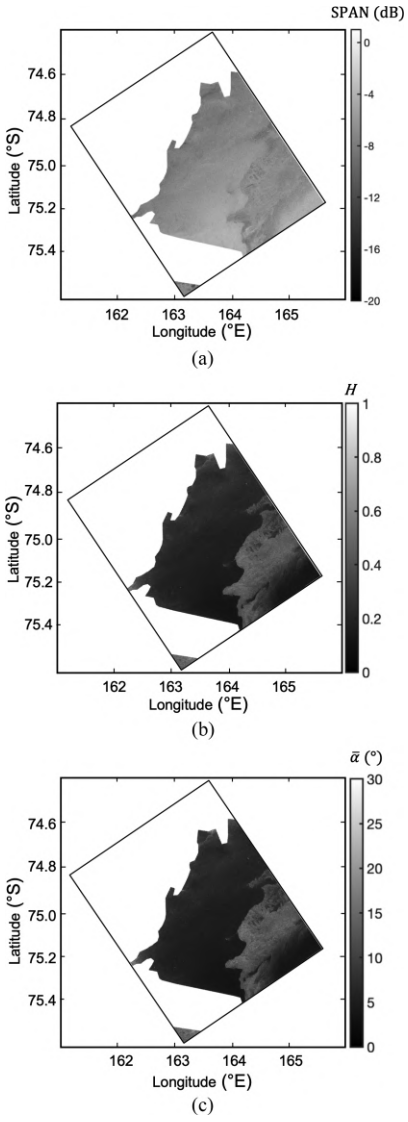


Fig. 12. Graytones images showing (a) the SPAN (dB), (b) the $H$, and (c) the $\bar{\alpha}$ (°) features. Land ice is masked in white.

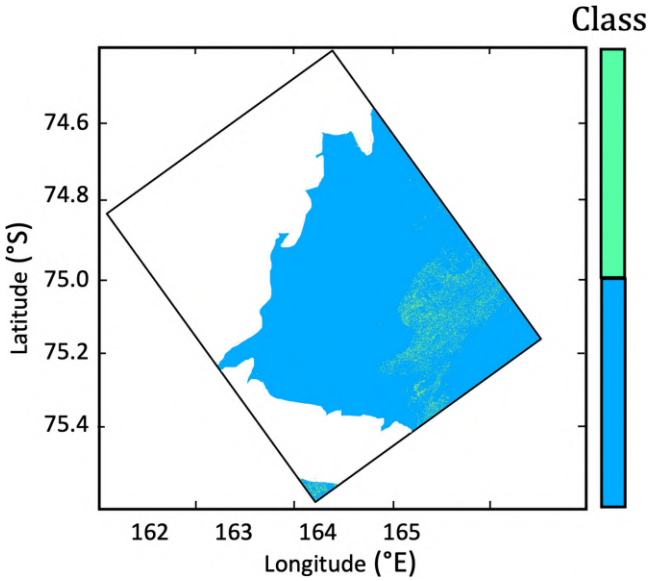


Fig. 13. Unsupervised Wishart $H/\bar{\alpha}$ output. Land ice is masked in white.

images that refer to SPAN (dB), $H$, and $\bar{\alpha}$ (°), are displayed in Fig. 12(a) and 12(c), respectively. There is no hint of signal that can be associated to the polynya; while the ice-free sea surface is distinguishable from sea ice. The sea water results in SPAN ($H$ and $\bar{\alpha}$) values larger (lower) than the offshore sea ice. The mean and standard deviation values evaluated over the selected sea water ROI for both incoherent and coherent features show almost the same trend observed for the previous experiments, see Table II. The unsupervised Wishart $H/\bar{\alpha}$ classifier output image is shown in Fig. 13, where the TNB area again belongs to the light blue color class, demonstrating consistency with the previous experiments. The output image also shows a second class, displayed in bright green color, which well matches with the sea ice surrounding the TNB area.

## V. Conclusion

In this study, the TNB coastal polynya is observed, under different environmental conditions, by dual-polarization RS-2 C-band SAR measurements using coherent and incoherent features. The analysis is supported, when available, by independent space/time collocated optical remote sensing images acquired by the MODIS sensor and by ancillary information obtained by two on-site AWSs. Experimental results show that the cross-polarized channel provides complementary information with respect to the conventional copolarized channel that can be used to better distinguish sea ice from the surrounding sea. In addition, coherent dual-polarimetric features can be used to support a fine-resolution characterization of the inhomogeneities within the polynya. The main outcomes can be summarized as follows.

1) SAR imagery is a key source of information to effectively observe the TNB coastal polynya thanks to its fine spatial resolution and almost continuous imaging capabilities.
2) The two polarimetric channels provide complementary information that can be jointly used to perform a finer-resolution classification of the polynya.
3) The coherent polarimetric features perform better than the incoherent ones to discriminate ice-free from sea-ice-infested areas within the polynya.
4) The TNB polynya extent and the sea-water fractional area coverage can be estimated in an unsupervised, accurate, and robust way by using the Wishart decomposition.

The outcomes of this study provide new insights on the multipolarization scattering signatures of ice-free and ice-infested TNB polynya at C-band. They suggest to exploit polarimetric SAR satellites as a complementary tool able to provide fine spatial scale information useful for the continuous and updated monitoring of such harsh coastal environment. Those capabilities may be a key asset for maritime surveillance and marine domain awareness.

In the future, we plan to exploit polarimetric C-band SAR measurements to identify the different phases of polynyas, i.e., opening/closing, and to provide further insights on the different multipolarization backscattering response of the different types of sea ice, including frazil, grease, and pancake ice. In addition, the consistency of our results with respect to other coastal polynyas characterized by different metocean conditions will be investigated.

## Acknowledgment

The authors would like to thank the Canadian Space Agency for providing RS-2 SAR data under the SOAR-EU project ID 16313 entitled “Multipolarization SAR for sea ice monitoring.”

## References

[1] S. Martin, “Polynyas,” in *Encyclopedia of Ocean Sciences*, vol. 4, Amsterdam, The Netherlands: Elsevier, 2011, pp. 540–545.
[2] S. Kern, “Wintertime Antarctic coastal polynya area: 1992–2008,” *Geophysical Res. Lett.*, vol. 36, 2009, Art. no. L14501.
[3] R. Drucker, S. Martin, and R. Moritz, “Observations of ice thickness and frazil ice in the ST Lawrence Island polynya from satellite imagery, upward looking sonar, and salinity/temperature moorings,” *J. Geophysical Res.*, vol. 108, no. C5, pp. 3149–3166, 2003.
[4] L. Thompson, M. Smith, J. Thomson, S. Stammerjohn, S. Ackley, and B. Loose, “Frazil ice growth and production during katabatic wind events in the Ross Sea Antarctica,” *Cryosphere*, vol. 14, pp. 3329–3347, 2020.
[5] K. Nakata, K. I. Ohshima, and S. Nihashi, “Mapping of active frazil for antarctic coastal polynyas, with an estimation of sea-ice production,” *Geophysical Res. Lett.*, vol. 48, no. 6, 2021, Art. no. e2020GL091353.
[6] P. Wadhams, G. Aulicino, F. Parmiggiani, P. O. G. Persson, and B. Holt, “Pancake ice thickness mapping in the Beaufort Sea from wave dispersion observed in SAR imagery,” *J. Geophysical Res. Ocean*, vol. 123, no. 3, pp. 2213–2237, 2018.
[7] G. Fusco, G. Budillon, and G. Spezie, “Surface heat fluxes and thermohaline variability in the Ross Sea and in Terra Nova Bay polynya,” *Continental Shelf Res.*, vol. 29, no. 15, pp. 1887–1895, 2009.
[8] T. Tamura, K. I. Ohshima, and S. Nihashi, “Mapping of sea ice production for Antarctic coastal polynyas,” Geophysical Res. Lett., vol. 35, 2008, Art. no. L07606.
[9] H. Han and H. Lee, “Glacial and tidal strain of landfast sea ice in Terra Nova Bay, East Antarctica, observed by interferometric SAR techniques,” Remote Sens. Environ., vol. 209, pp. 41–51, 2018.
[10] T. Tamura, K. I. Oshima, A. D. Fraser, and G. D. Williams, “Sea ice production variability in Antarctic coastal polynyas,” *J. Geophysical Res. Oceans*, vol. 121, pp. 2967–2979, 2016.
[11] E. Rusciano, G. Budillon, G. Fusco, and G. Spezie, “Evidence of atmosphere-sea ice-ocean coupling in the Terra Nova Bay polynya,” *Cont. Shelf Res.*, vol. 61–62, pp. 112–124, 2013.
[12] C. L. Stewart, P. Christoffersen, K. W. Nicholls, M. J. M. Williams, and J. A. Dowdeswell, “Basal melting of Ross Ice Shelf from solar heat absorption in an ice-front polynya,” Nature Geosci., vol. 12, pp. 435–440, 2019.
[13] K. I. Ohshimaet al., “Antarctic a-ice formation in the Cape Darnley polynya,” Nature Geosci., vol. 6, pp. 235–240, 2013.
[14] T. Hollands and W. Dierking, “Dynamics of the Terra Nova Bay polynya: The potential of multi–sensor satellite observations,” *Remote Sens. Env*, vol. 187, pp. 30–48, 2016.
[15] S. Paul, S. Willmes, and G. Heinemann, “Long-term coastal-polynya dynamics in the southern Weddell Sea from MODIS thermal-infrared imagery,” *Cryosphere*, vol. 9, pp. 2027–2041, 2015.
[16] A. Preußer, G. Heinemann, S. Willmes, and S. Paul, “Multi-decadal variability of polynya characteristics and ice production in the North water polynya by means of passive microwave and thermal infrared satellite imagery,” *Remote Sens.*, vol. 7, no. 12, pp. 15844–15867, 2015.
[17] S. Nihashi, K. I. Ohshima, and T. Tamura, “Sea-ice production in Antarctic coastal polynyas estimated from AMSR2 data and its validation using AMSR-E and SSM/I-SSMIS data,” IEEE J. Sel. Topics Appl. Earth Observ. Remote Sens., vol. 10, no. 9, pp. 3912–3922, Sep. 2017.
[18] L. Jianget al., “Trends in the stability of Antarctic coastal polynyas and the role of topographic forcing factors,” *Remote Sens.*, vol. 12, 2020, Art. no. 1043.
[19] G. Aulicino, G. Fusco, S. Kern, and G. Budillon, “Estimation of sea-ice thickness in Ross and Weddell Seas from SSM/I brightness temperatures,” *IEEE Trans. Geosci. Remote Sens.*, vol. 52, pp. 4122–4140, Jul., 2014.
[20] J. C. Comiso, R. Kwok, S. Martin, and A. L. Gordon, “Variability and trends in sea ice extent and ice production in the Ross Sea,” *J. Geophysical Res.*, vol. 116, 2011, Art. no. C04021.
[21] S. Nihashi and K. I. Ohshima, “Circumpolar mapping of Antarctic coastal polynyas and landfast sea ice: Relationship and variability,” *J. Climate*, vol. 28, no. 9, pp. 3650–3670, 2015.
[22] M. Sansiviero, M. A. Morales Maqueda, G. Fusco, G. Aulicino, D. Flocco, and G. Budillon, “Modelling sea ice formation in the Terra Nova Bay polynya,” *J. Mar. Syst.*, vol. 4, pp. 1–25, 2017.
[23] A. Ciappa, L. Pietranera, and G. Budillon, “Observations of the Terra Nova Bay (Antarctica) polynya by MODIS ice surface temperature imagery from,” Remote Sens. Environ., vol. 119, pp. 158–172, 2012.
[24] J. H. Cho, J. M. Cho, H. S. Yun, T. W. Kim, and C. W. Kim, “A study of shoreline changes in Antarctica (Terra Nova Bay) based on SAR data,” in *Proc. 12th Int.l Coastal Symp.*, Plymouth, England, 2013, no. 65, pp. 2101–2106, doi: 10.2112/SI65-355.1.
[25] G. Aulicinoet al., “A new approach for monitoring the Terra Nova Bay polynya through MODIS ice surface temperature imagery and its validation during 2010 and 2011 winter seasons,” *Remote Sens.*, vol. 10, no. 3, 2018, Art. no. 366.
[26] M. Zahriban Hesari, F. Nunziata, G. Aulicino, A. Buono, and M. Migliaccio, “Analysis of fine-scale dynamics of the Drygalski ice tongue in Antarctica using satellite SAR data,” *Int. J. Remote Sens.*, vol. 43, no. 7, pp. 2581–2598, 2022.
[27] A. Ciappa and L. Pietranera, “High resolution observations of the Terra Nova Bay polynya using COSMO–SkyMed X–SAR and other satellite imagery,” *J. Mar. Syst.*, vol. 113–114, pp. 42–51, 2013.

[28] F. Parmiggiani, "Fluctuations of Terra Nova Bay polynya as observed by active (ASAR) and passive (AMSR–E) microwave radiometers," *Int. J. Remote Sens.*, vol. 27, pp. 2459–2467, 2006.

[29] M. Moctezuma, F. Parmiggiani, and L. Lopez, "Automatic measurement of polynya area by anisotropic filtering and Markov random fields," *IEEE J. Sel. Topics Appl. Remote Sens.*, vol. 7, no. 5, 1665–1674, May 2014.

[30] K. Ji and Y. Wu, "Scattering mechanism extraction by a modified Cloude-Pottier decomposition for dual polarization SAR," *Remote Sens.*, vol. 7, pp. 7447–7470, 2015.

[31] Z. Shan, C. Wang, H. Zhang, and J. Chen, "H-$\alpha$ decomposition and alternative parameters for dual polarization SAR data," in *Proc. PIERS*, Suzhou, China, 2011, pp. 1386–1390.

[32] S. Cloude, "The dual polarisation entropy/alpha decomposition: A PalSAR case study," in *Proc. PolInSAR*, Frascati, Italy, 2007, pp. 1–6.

[33] S. R. Cloude and E. Pottier, "A review of target decomposition theorems in radar polarimetry," *IEEE Trans. Geosci. Remote Sens.*, vol. 34, no. 2, pp. 498–518, Mar. 1996.

[34] D. L. Schuler and J. S. Lee, "Mapping ocean surface features using biogenic slick-fields and SAR polarimetric decomposition techniques," *Proc. Radar, Sonar Navigation*, vol. 153, no. 3, pp. 260–270, 2006.

[35] A. Buono, C. R. De Macedo, F. Nunziata, D. Velotto, and M. Migliaccio, "Analysis on the effects of SAR imaging parameters and environmental conditions on the standard deviation of the co-polarized phase difference measured over sea surface," *Remote Sens.*, vol. 11, 2019, Art. no. 18.

[36] S. V. Nghiem, R. Kwok, S. H. Yue, and M. R. Drinkwater, "Polarimetric signatures of sea ice: 2. Experimental observations," J. Geophysical Res., vol. 100, pp. 13681–13698, 1995.

[37] H. Li and W. Perrie, "Sea ice characterization and classification using hybrid polarimetry SAR," IEEE J. Sel. Topics Appl. Remote Sens., vol. 9, no. 11, 4998–5010, Nov. 2016.

[38] J.-S. Lee, M. R. Grunes, T. L. Ainsworth, L.-J. Du, D. L. Schuler, and S. R. Cloude, "Unsupervised classification using polarimetric decomposition and the complex Wishart classifier," *IEEE Trans. Geosci. Remote Sens.*, vol. 37, no. 5, pp. 2249–2258, Sep. 1999.

[39] L. Ferro-Famil, E. Pottier, and Jong-Sen Lee, "Unsupervised classification of multi-frequency and fully polarimetric SAR images based on the H/A/Alpha-Wishart classifier," IEEE Trans. Geosci. Remote Sens., vol. 39, no. 11, pp. 2332–2342, Nov. 2001.

[40] W. Wang, D. Xiang, J. Zhang, and J. Wan, "Integrating contextual information with $H/\bar{\alpha}$ decomposition for PolSAR data classification," *IEEE Geosci. Remote Sens. Lett.*, vol. 13, no. 12, pp. 2034–2038, Dec. 2016.

[41] A. Buono, F. Nunziata, M. Migliaccio, X. Yang, and X. Li, "Classification of the Yellow River delta area using fully polarimetric SAR measurements," Int. J. Remote Sens., vol. 38, no. 23, pp. 6714–6734, 2017.

[42] F. Goudail and P. Refregier, "Contrast definition for optical coherent polarimetric images," IEEE Trans. Pattern Anal. Mach. Intell., vol. 26, no. 7, pp. 947–951, Jul. 2004.

[43] J. Morio, P. Refregier, F. Goudail, P. C. Dubois-Fernandez, and X. Dupuis, "A characterization of Shannon entropy and Bhattacharyya measure of contrast in polarimetric and interferometric SAR image," *Proc. IEEE*, vol. 97, no. 6, pp. 1097–1108, Jun. 2009.

[44] F. Nunziata, A. Buono, and M. Migliaccio, "Cosmo-SkyMed synthetic aperture radar data to observe the Deepwater Horizon oil spill," *Sustainability*, vol. 10, no. 10, 2018, Art. no. 3599.


**Giovanna Inserra** (Student Member, IEEE) was born in Gragnano, Italy, in 1987. She received the B.Sc. and M.Sc. degrees in telecommunication engineering, in 2016 and 2010, respectively, from the Università degli Studi di Napoli "Parthenope," Napoli, Italy, where she is currently working toward the Ph.D. degree in information and communication technology and engineering.

Her research interests include the exploitation of multipolarization synthetic aperture radar measurements to observe harsh coastal environments.

**Andrea Buono** (Senior Member, IEEE) was born in Napoli, Italy, in 1984. He received the B.Sc. and M.Sc. degrees in telecommunication engineering and the Ph.D. degree in information engineering from the Università di Napoli "Parthenope, Napoli, Italy, in 2010 and 2013, respectively, in 2017.

Since 2018, he has been Assistant Professor of Electromagnetics with Università degli Studi di Napoli "Parthenope." His research interests include applied electromagnetics, including electromagnetic modeling, polarimetry, ocean and coastal area applications.

**Ferdinando Nunziata** (Senior Member, IEEE) was born in Avellino, Italy, in 1982. He received the B.Sc., M.Sc., and Ph.D. degrees in telecommunication engineering from the Università degli Studi di Napoli "Parthenope," Napoli, Italy, in 2003, 2005, and 2008, respectively.

Since 2019, he has been Associate Professor with Università degli Studi di Napoli "Parthenope." His research interests include applied electromagnetics, i.e., sea surface scattering, radar polarimetry, SAR sea oil slick and metallic target monitoring, spatial resolution enhancement techniques, and GNSS-R.

**Maurizio Migliaccio** (Fellow IEEE) was born in Napoli, Italy, in 1962. He received the laurea degree (Hons.) in electronic engineering from the Università di Napoli Federico II, Napoli, Italy, in 1987.

He is currently a Full Professor of Electromagnetics with the Università degli Studi di Napoli "Parthenope," Napoli, Italy. His research interests include remote sensing for marine and coastal applications, polarimetry, inverse problem for resolution enhancement, and reverberating chambers.

**Flavio Parmiggiani** was born in Campagnola Emilia, Italy, in 1945. He received the M.S. degree in physics from the University of Milan, Milan, Italy, in 1970.

From 1970 to 1982, he worked in the field of biological cybernetics (moto-neuron models and motor control) with the Italian National Research Council (CNR), Milan, Italy. From 1978 to 1980, he spent two years with the Laboratory of Neurophysiology, University of Alberta, Edmonton, AB, Canada, on a NATO Fellowship. In 1982, he joined a new CNR Institute, IMGA-CNR, later ISAC–CNR, Bologna, Italy. From 1989 to 2012, he was responsible for the satellite receiving station of the Italian Base in Antarctica for real-time operations. In 2019, he joined the Institute of Polar Sciences-CNR. His research interests include glaciology and satellite image interpretation and classification.

**Giuseppe Aulicino** was born in Sorrento, Italy, in 1981. He received the M.Sc. degree in environmental sciences from the Università degli Studi di Napoli "Parthenope," Napoli, Italy, and the Ph.D. degree in polar sciences from the Univeristà degli Studi di Siena, Siena, Italy, in 2007 and 2011, respectively.

He is currently Assistant Professor of Oceanography and Physics of the Atmosphere with the Università degli Studi di Napoli "Parthenope." His research interests include remote sensing and oceanographic modeling for cryosphere.